THE ASTROPHYSICAL JOURNAL, 563:289–300, 2001 December 10

HOLLOW ACCRETION COLUMNS ON NEUTRON STARS AND THE EFFECTS OF GRAVITATIONAL LIGHT BENDING

U. KRAUS
Theoretische Astrophysik, Universität Tübingen, Auf der Morgenstelle 10C, Tübingen D-72076, Germany; kraus@tat.physik.uni-tuebingen.de
Received 2000 November 27; accepted 2001 August 14

ABSTRACT

This study investigates the beam patterns for radiation originating in a hollow column on a slowly rotating neutron star where the Schwarzschild metric is appropriate for calculating photon paths. The beam pattern of a hollow column is the sum of contributions from the two emitting surfaces on the inside and the outside of the column, which combine into a two-component beam pattern. The shapes of the inside beam pattern, the outside beam pattern, and the combined beam pattern are studied for radial cones of different height and width, for isotropic and beamed emission, and for different values of mass and radius of the neutron star. It is argued that the hollow cone model provides an interpretation of the pulse profiles of the X-ray pulsar Centaurus X-3.

Subject headings: gravitational lensing — pulsars: general — pulsars: individual (Centaurus X-3) — stars: neutron — X-rays: binaries

1. INTRODUCTION

The standard model of a binary X-ray pulsar is that of a close binary system in which a strongly magnetized neutron star accretes matter from its nondegenerate companion. The X-radiation originates in a region close to or on the stellar surface where the infalling matter decelerates. Because of the strong magnetic field of the neutron star, the accreted matter is funneled toward the magnetic poles, so X-ray emission is confined to two small emission regions. Therefore, when the neutron star rotates the X-ray flux appears pulsed to a distant observer.

The pulse profiles of accreting X-ray pulsars, their dependence on photon energy, and their variation with X-ray luminosity are characteristic for each source. Since the details of the accretion flow and the radiation field in the emission regions are still imperfectly understood, studies of simplified models may help to interpret qualitatively the features observed in the pulse profiles and to obtain a better understanding of the properties of the emission regions.

One important aspect concerning the emission regions is the accretion geometry. Together with relativistic light deflection near the neutron star, it has a major influence on the predicted pulse shapes. The accretion geometry is determined by the filling factor of the accretion funnel and the mode of deceleration. If the threading region of the accretion disk where matter latches onto the magnetic field lines has an extension that is small compared to the Alfvén radius, then the accretion funnel is expected to be a thin-walled hollow column. A large threading region should result in a filled funnel. If the deceleration of the infalling matter occurs in the neutron star atmosphere, then the emission region is essentially a part of the stellar surface. This emitting slab is in the shape of a polar cap if the funnel is filled and in the shape of a ring for a hollow funnel. If, on the other hand, the matter decelerates at some distance above the surface because of a shock or radiation pressure, the emission region is an accretion column, either filled or hollow.

The beam patterns arising from radiating hot spots on the surface of the neutron star have been investigated by Pechenick, Ftaclas, & Cohen (1983). They considered isotropic and beamed emission, different cap sizes, and different values for the mass and radius of the neutron star. Riffert et al. (1993) and Leahy & Li (1995) considered polar caps and rings and performed fits to observed pulse profiles in order to determine the locations of the caps or rings on the neutron star surface as well as the viewing direction. Riffert & Mészáros (1988) studied the beam patterns of radial cones radiating from the sides and the dependence on the height of the cone and on mass and radius of the neutron star.

This study complements the ones by Pechenick, Ftaclas, & Cohen (1983) and by Riffert & Mészáros (1988) with an investigation of the beam patterns of hollow cones. The new feature of a hollow cone model that is not present in the polar cap, polar ring, and column models is the fact that there are contributions from two emitting surfaces with different physical conditions in general that combine to a two-component beam pattern. Section 2 contains the description of the simple geometrical model on which this study is based and of the method used for the computation of the beam patterns. The shapes of the inner, the outer, and the combined beam patterns are studied in § 3 for cones of different height and width, for isotropic and beamed emission, and for different values of mass and radius of the neutron star. It is argued in § 4 that the pulse profile of the X-ray pulsar Cen X-3 lends itself to an interpretation in terms of a hollow accretion column.

2. ACCRETION COLUMN MODEL AND COMPUTATION OF THE BEAM PATTERNS

Studies of the dynamic infall problem of matter accreting onto a neutron star in a narrow funnel have shown that in high-luminosity sources, the matter is decelerated above the stellar surface in a radiative shock that separates a region of freely falling plasma above from a settling region of nearly stagnant plasma below, with radiation mainly originating in the deceleration and settling regions and escaping from the sides of the column (Basko & Sunyaev 1976; Wang & Frank 1981; Kirk 1985; Arons 1992; Becker 1998). The

radiative shock in a thin-walled hollow funnel is expected to rise above the stellar surface if the luminosity L exceeds L_*:

$$L > L_* = \frac{\alpha}{4} L_{\rm Edd} \frac{\sigma_{\rm T}}{\sigma_s}, \quad (1)$$

where α is the half-opening angle of the base of the funnel, $L_{\rm Edd} = 4\pi c m_p GM/\sigma_{\rm T}$ the Eddington luminosity, M the mass of the neutron star, $\sigma_{\rm T}$ the Thomson scattering cross section, and σ_s the magnetic scattering cross section averaged over direction and frequency (Basko & Sunyaev 1976). The radiation observed from a hollow column originates from the inner and outer walls of the optically thick settling mound below the shock. These two emission regions differ in their visibility for a distant observer. While the outer wall is either directly visible or hidden behind the neutron star, the inner wall may be directly visible (if the line of sight is close to the magnetic axis), visible across the free-fall region, or hidden by the optically thick settling region. The optical depth across the base of the free-fall region at radial coordinate r is

$$\tau_\perp = \frac{\rho d\sigma}{m_p} \approx 2 \frac{L}{L_*} \frac{\sigma}{\sigma_s} \sqrt{\frac{r_n}{r}} \sqrt{\frac{r_n}{10\ {\rm km}}} \sqrt{\frac{M_\odot}{M}}, \quad (2)$$

where ρ is the average density, d the thickness of the column wall, σ the magnetic scattering cross section, and r_n the radius of the neutron star. For $L \gtrsim L_*$ and Thomson (nonmagnetic) scattering ($\sigma = \sigma_T = \sigma_s$), the free-fall region is marginally optically thick; for higher luminosities increasingly so. For magnetic scattering in the strong magnetic field B of an X-ray pulsar, σ greatly exceeds $\sigma_{\rm T}$ near the cyclotron resonance and may be reduced far below $\sigma_{\rm T}$ for low frequencies $\omega \ll \omega_c = eB/m_e$. The low-frequency scattering cross section is to a good approximation given by

$$\sigma_1 = \sigma_{\rm T}\left[\sin^2 \vartheta + \cos^2 \vartheta \left(\frac{\omega}{\omega_c}\right)^2\right], \quad \sigma_2 = \sigma_{\rm T}\left(\frac{\omega}{\omega_c}\right)^2 \quad (3)$$

for the ordinary and extraordinary modes of polarization, respectively, where ϑ is the angle between the direction of propagation of the radiation and the magnetic field (Arons & Klein 1987), so the free-fall region is optically thin to low-frequency radiation in the extraordinary mode. At higher frequencies the free-fall region will increasingly be optically thick for both polarization modes. Therefore, one must expect that radiation from the inner column wall makes an important contribution to the beam pattern at low frequencies and that scattering of inner wall radiation in the free-fall zone makes an impact on the energy and luminosity dependence of the beam pattern.

In the following, a simple geometrical model will be used in order to point out the main characteristics of the two-component beam pattern arising from a hollow column. Emphasis will be on the impact of relativistic light deflection near the neutron star on the visibility of the emitting column walls and thereby on the beam pattern. In this model (sketched in Fig. 1) the neutron star with Schwarzschild radius $r_{\rm S} = 2GM/c^2$ and radius r_n is assumed to be slowly rotating so that the Schwarzschild metric is appropriate for calculating photon paths. The shape of the accretion funnel is approximated as a radial cone with inner and outer half-opening angles α_i and α_o, respectively. Below a radiative shock at radial coordinate r_t the column is optically thick and radiation is emitted from the inner and outer walls. Details of the moundlike inner structure of this region are not taken into account. The emission is either assumed to be isotropic or to be a function $I(\delta)$ of the angle δ between the direction of emission and the radial direction (which, in the approximation of a radial cone, represents the direction of the magnetic field that is also the direction of motion of the accreted matter). The free-fall region above the shock is treated as being optically thin both to free-free absorption and to scattering. This represents the limiting case of optimum visibility of the inner emission region that is appropriate for low-frequency radiation in the extraordinary mode. This limiting case is useful to point out the main characteristics of the two-component beam pattern as opposed to the other limiting case of complete obscuration of the inner emission region that corresponds to the beam patterns of the outsides of columns investigated by Riffert & Mészáros (1988). Between the emission at radial coordinate r and the detection by an observer at the distance $d \gg r_{\rm S}$ the frequency of the radiation is redshifted according to

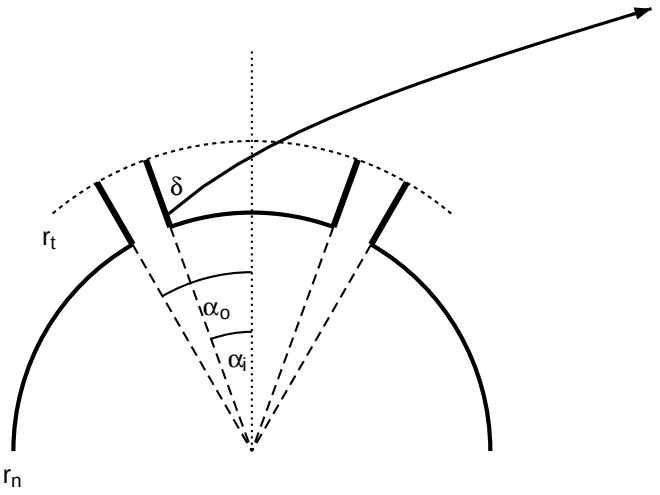

FIG. 1.—Hollow cone model of the emission region. A radial hollow cone with inner and outer half-opening angles α_i and α_o, respectively, and its top at the radial coordinate $r_{\rm T}$ radiates from the sides. The emission is either assumed to be isotropic or to be a function $I(\delta)$ of the angle δ between the direction of emission and the radial direction. Photon paths are calculated in the Schwarzschild metric. In the drawing, the height and width of the cone have been exaggerated for clarity.

$$\omega_\infty = \omega \sqrt{1 - \frac{r_{\rm S}}{r}} \quad (4)$$

and the specific intensity changes according to

$$I_\infty(\omega_\infty) = \left(\frac{\omega_\infty}{\omega}\right)^3 I(\omega) \quad (5)$$

(Misner, Thorne, & Wheeler 1973). If the cone is small enough, then redshift and intensity change are approximately constant over the whole emission region. In the computations presented below for phenomenological emission models on small cones (where no attempt is made to investigate a dependence of the emission on height), redshift and intensity change are taken to be constant. Their effect is then to introduce an overall scale factor into the beam pattern which is not taken into account in the results shown below. If required for a more detailed emission model or a taller cone, the position-dependent redshift and intensity change can easily be incorporated into the computation.

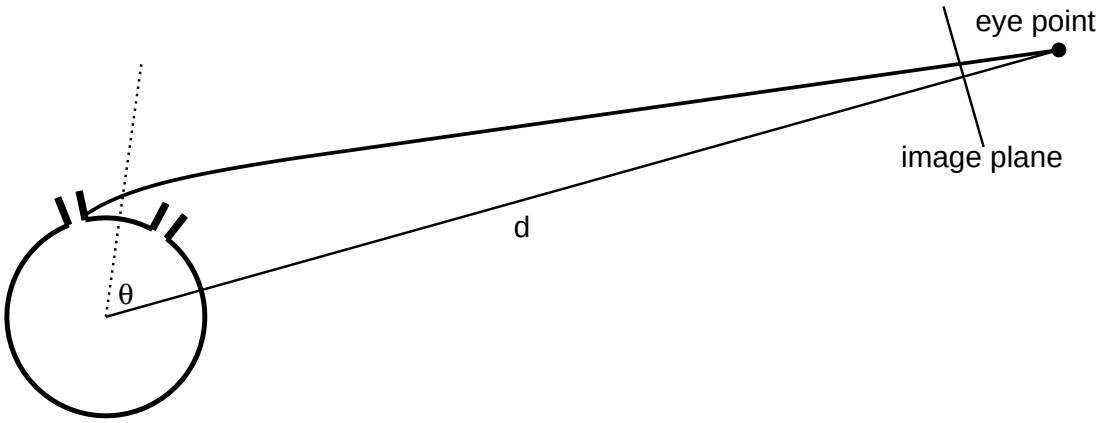

FIG. 2.—Ray-casting method. The paths of light rays are retraced from a distant observer at $d \gg r_S$ to the emission points on the cone. The total flux is obtained by summing up the flux contained in the resolved image. The total flux is a function of the viewing angle θ. In the drawing, the height and width of the cone have been exaggerated for clarity.

When the neutron star rotates, the viewing angle θ onto the magnetic pole number i changes with rotation angle Φ according to

$$\cos\theta = \cos\Theta_o \cos\Theta_i + \sin\Theta_o \sin\Theta_i \cos(\Phi - \Phi_i) , \quad (6)$$

where Θ_o is the angle between the axis of rotation and the line of sight, Θ_i is the angular distance of magnetic pole number i from the rotation axis, and $\Phi = \Phi_i$ is the instant when the axis through pole i passes closest to the direction of observation. When the observed flux of the emission region as a function of θ, i.e., the beam pattern, is known, then pulse shapes can be calculated for arbitrary geometric parameters. The computation of the beam pattern is done here using ray-tracing. Ray-tracing is a standard technique in computer graphics (Foley et al. 1990) which has been modified to include relativistic light deflection (Nollert et al. 1989; Zahn 1991; Weiskopf 2000). For each value of θ a resolved image of the emission region is computed by retracing the paths of light rays reaching a hypothetical screen (see Fig. 2). When retracing the path leads to a point on an emitting surface, the specific intensity reaching the respective point on the screen is computed from the point and the direction of emission. The total flux detected from viewing angle θ is then obtained by summing up the flux contained in the image.

The accuracy of the numerical computation was tested by the comparison with analytically computed beam patterns for $r_S = 0$ (no light deflection) and isotropic emission. In this case, the observed flux is proportional to the projected area of the unshadowed part of the emitting surfaces. Figure 3 shows two comparisons for the inside component and the outside component of a beam pattern, respectively, with the parameter values $r_t = 1.05\ r_n$, $\alpha_i = 0.1$, and $\alpha_o = 0.1$. The formulae for the analytic beam patterns are given in the Appendix.

An emission region model is characterized by four geometric parameters and the beaming function:

$$\frac{r_n}{r_S}, \frac{r_t}{r_S}, \alpha_i, \alpha_o, I(\omega, \delta) .$$

The computational expense in exploring this parameter space can be reduced by using the beam patterns computed for isotropic emission as transfer functions for an approximate computation of the beam patterns for beamed emission. This is based on the observation that radiation emitted with angles δ in some small range $\delta_1 \le \delta \le \delta_2$ contributes to the beam pattern only in a small range in θ (see Fig. 4). The relation between corresponding values of δ and θ can be obtained by computing a single representative light ray for each pair of angles. The values shown in Figure 4

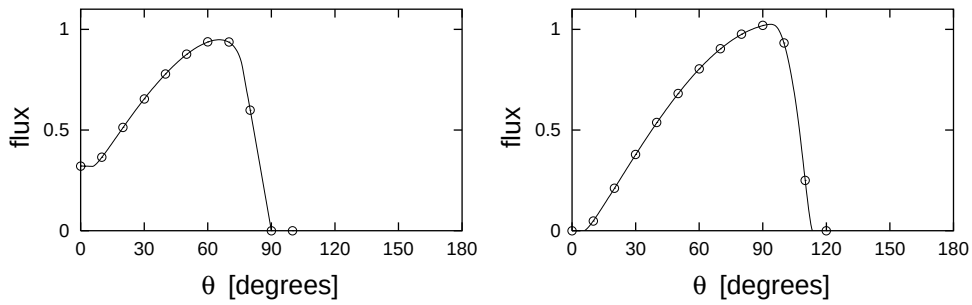

FIG. 3.—Comparison between analytically computed beam patterns (*solid lines*) and values computed by ray-casting (*symbols*) for $r_S = 0$ and isotropic emission. Left: beam pattern due to the inside of a radial cone with $r_t/r_n = 1.05$, $\alpha_i = 0.1$. Right: beam pattern due to the outside of a radial cone with $r_t/r_n = 1.05$, $\alpha_o = 0.1$.

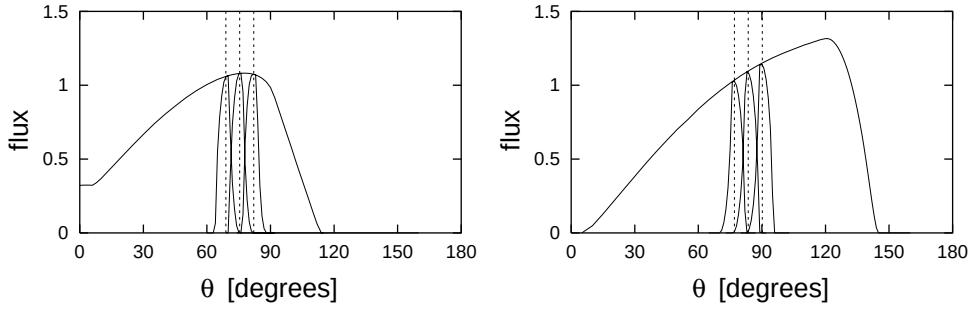

FIG. 4.—Radiation emitted with angles δ (between the direction of emission and the radial direction) in a small δ-range contributes to the beam pattern only in a small range of viewing angles θ. The δ-ranges shown are 5° wide and are centered on $\delta = 60°$, 65°, and 70°. The dashed lines mark the values of θ computed for three representative light rays as described in the text with $\delta = 60°$, 65°, and 70°. *Left*: inner component, *right*: outer component of the beam pattern. The parameters are $r_n/r_S = 3.3$, $r_t/r_n = 1.05$, $\alpha_i = 0.1$, and $\alpha_o = 0.1$.

(*dashed lines*) have been computed for light rays with δ in the middle of the δ-ranges considered and starting midway between r_n and r_t at 45° out of the plane of the cone axis and the observer. These values agree quite well with the maxima of the contributions of the respective small δ-ranges. The computation of the approximate beam patterns for beamed emission then proceeds as follows: for each value of θ one computes the corresponding value of δ. The flux in the beam pattern for isotropic emission $F_{\rm iso}(\theta)$ is then scaled with the beaming function $I(\delta)$ to yield the flux in the beam pattern for nonisotropic emission

$$F_{I(\delta)}(\theta) = F_{\rm iso}(\theta) I(\delta(\theta)) \; . \tag{7}$$

Figure 5 gives a comparison between a full and an approximate computation of the beam patterns for $I(\delta) = \sin^4 \delta$ for the inner and outer components of the beam pattern separately.

3. RESULTS

In generating the following results, the parameters have been chosen in a range that may be suitable for X-ray pulsar models. Starting from a basic model with $r_n/r_S = 3.3$, $r_t = 1.05 r_n$, $\alpha_i = 0.1$, $\alpha_o = 0.1$, and isotropic emission, the parameters are varied one at a time to display the influence that each one has on the shape of the beam pattern.

3.1. *Inside Component of the Beam Pattern*

Figure 6 shows the contribution that the inside of the cone makes to the beam pattern of the basic model. For comparison it also shows the beam pattern obtained for the same geometry but with $r_S = 0$ (i.e., no light deflection). At the smallest values of θ the two curves are nearly identical. This is the result of the fact that light rays emitted nearly radially suffer very little light deflection. The nonrelativistic beam pattern drops to zero at $\theta = 90°$ when the inside of the cone disappears from view. Light deflection shifts this point of disappearance toward larger values of θ while preserving the rapid decline of the flux.

The dependence of the inside beam pattern on the mass of the neutron star is further illustrated in the left column of Figure 7 with beam patterns for $r_n/r_S = \infty$, 3.3, 2.5, 2.2, 2.1, and 2. When r_S is larger, both the flux maximum and the point of disappearance are shifted toward larger values of θ.

In the middle column of Figure 7 the beam pattern of the basic model is compared to beam patterns of cones that have opening angles half and twice as large. In this case, the position of the flux maximum changes, but the point of disappearance is virtually independent of the opening angle.

The influence of the cone height on the inside beam pattern is considered in the right column of Figure 7 for $r_t/r_n = 1.1$, 1.05, and 1.01. The position of the flux maximum changes with cone height, but the point of disappearance remains nearly the same.

3.2. *Outside Component of the Beam Pattern*

The contribution that the outside of the cone makes to the beam pattern is shown in Figure 8 for the same param-

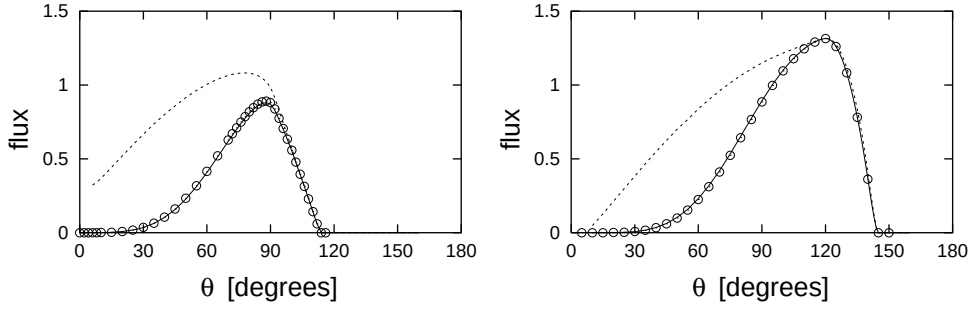

FIG. 5.—Comparison between approximate and full calculations of a beam pattern for beamed emission with $I(\delta) = \sin^4 \delta$. *Solid line*: approximate calculation based on the beam pattern for isotropic emission; *symbols*: full computation with ray-casting. *Dashed line*: beam pattern for isotropic emission. *Left*: inner component, *right*: outer component of the beam pattern. The geometric parameters are the same as in Fig. 4.

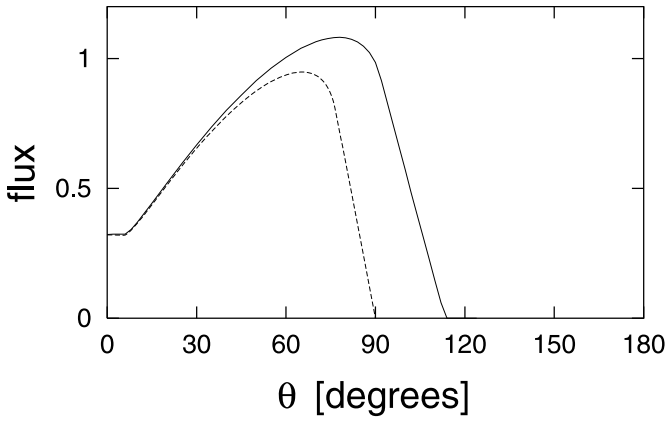

FIG. 6.—Inside component of the beam pattern of the "basic model" (*solid line*) in comparison with the $r_S = 0$ beam pattern for the same geometry (*dashed line*).

eter values that were used in Figure 7 for the inside beam pattern.

The position of both the flux maximum and the point at which the cone disappears behind the neutron star depend sensitively on the ratio r_n/r_S of the neutron star (Fig. 8, *left column*). If the star is sufficiently compact, the outside of the cone may even be visible from all directions. A change in opening angle or in cone height hardly changes the position of the flux maximum (Fig. 8, *middle and right columns*). In contrast to the inside beam pattern, however, opening angle and cone height here have a noticeable influence on the point of disappearance.

3.3. *Two-Component Beam Patterns*

Depending on how thin the matter-carrying region is, the inner opening angle may or may not be close to the outer one. For simplicity, and to avoid introducing another

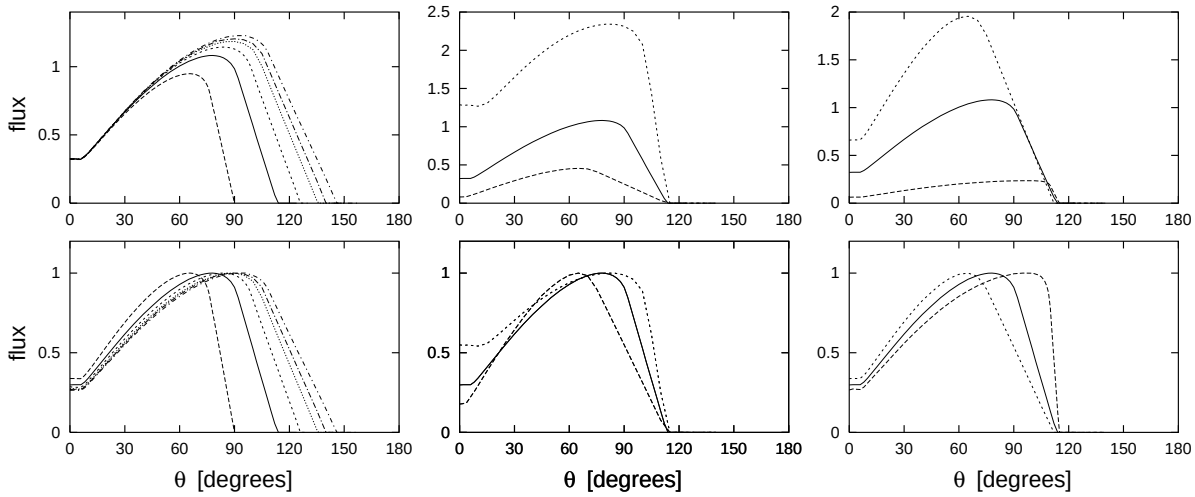

FIG. 7.—Inside component of the beam pattern for different parameter values. The upper plots show absolute values, the lower plots show the same curves normalized so that the maximum equals unity. *Left*: $r_n/r_S = \infty$, 3.3, 2.5, 2.2, 2.1, and 2 (*left to right*). *Middle*: $\alpha_i = 0.2$, 0.1, and 0.05 (*top to bottom*). *Right*: $r_t/r_n = 1.1$, 1.05, and 1.01 (*top to bottom*).

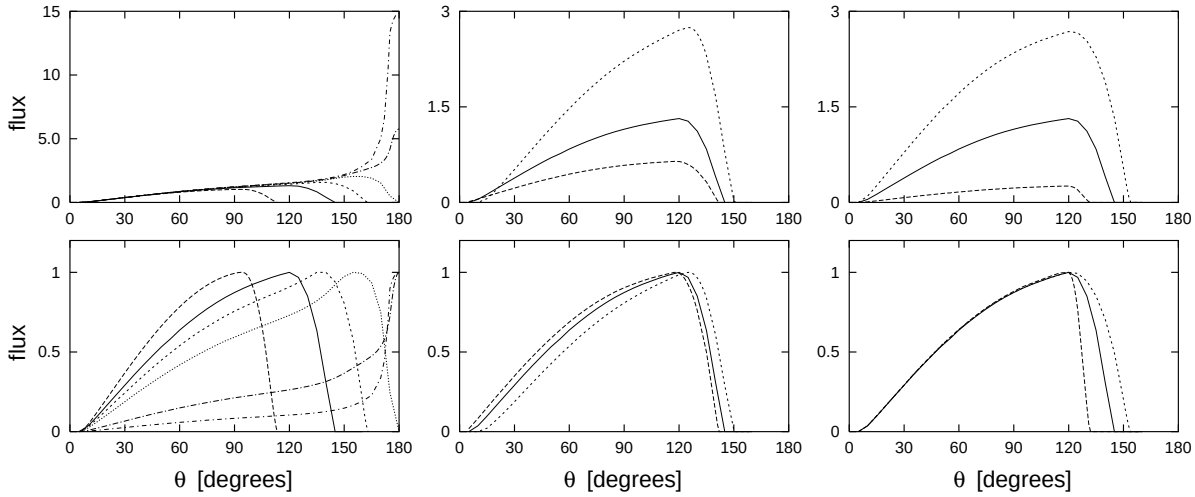

FIG. 8.—Outside component of the beam pattern for different parameter values. The upper plots show absolute values, the lower plots show the same curves normalized so that the maximum equals unity. *Left*: $r_n/r_S = \infty$, 3.3, 2.5, 2.2, 2.1, and 2 (*left to right*). *Middle*: $\alpha_i = 0.2$, 0.1, and 0.05 (*top to bottom*). *Right*: $r_t/r_n = 1.1$, 1.05, and 1.01 (*top to bottom*).

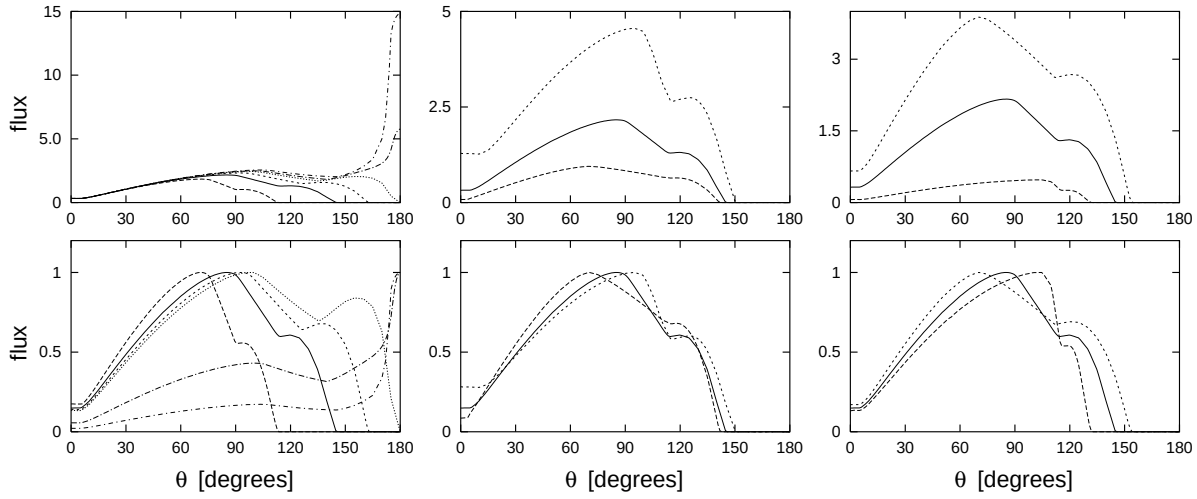

FIG. 9.—Two component beam patterns for different parameter values. The upper plots show absolute values, the lower plots show the same curves normalized so that the maximum equals unity. *Left*: $r_n/r_S = \infty$, 3.3, 2.5, 2.2, 2.1, and 2 (*left to right*). *Middle*: $\alpha_i = 0.2$, 0.1, and 0.05 (*top to bottom*). *Right*: $r_t/r_n = 1.1$, 1.05, and 1.01 (*top to bottom*).

parameter, the two-component beam patterns in this section are all computed in the limiting case of very thin column walls for $\alpha_i = \alpha_o$.

Figure 9 shows the complete beam patterns for the same sets of parameters that were considered in §§ 3.1 and 3.2. The inside and outside beam patterns add up to a two-component beam pattern with two maxima that may in some cases nearly blend into one broad peak.

3.4. *Beamed Emission*

Radiative transfer calculations in static atmospheres (Nagel 1981; Mészáros & Nagel 1985) suggest that the emission from the side of a column may be isotropic or may be enhanced in the direction perpendicular to the magnetic field. This is modeled here by the beaming functions

$$I_{\rm iso} = \text{const}\ , \quad I_1(\delta) = \sin^2\,\delta\ , \quad I_2(\delta) = \sin^4\,\delta\ . \qquad (8)$$

On the other hand, it has been suggested that high-velocity infall near the border of the accretion column may be optically thick and then cause substantial beaming by aberration (Lyubarskii & Syunyuaev 1988). Since this can only apply in a luminosity and frequency regime in which scattering in the free-fall region cannot be neglected, the computation of the inside beam patterns affected by aberration is strictly speaking outside the scope of this study, so that the inside beam patterns shown in Figure 10 can give only a rough indication of the expected effects of beaming. The computation of the outside beam patterns is not

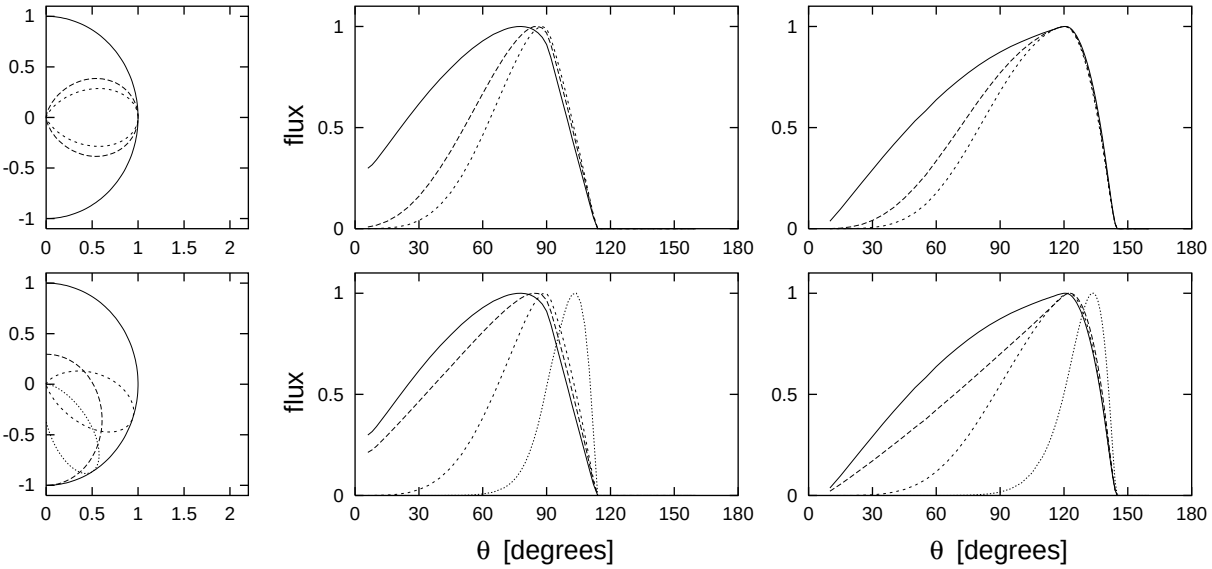

FIG. 10.—Beam patterns for beamed emission in comparison with beam patterns for isotropic emission. *Upper row*: beaming functions $I_{\rm iso}$ (*solid line*), I_1 (*dashed line*), and I_2 (*small dashes*). *Lower row*: beaming functions $I_{\rm iso}$ (*solid line*), I_3 ($\beta = 0.2$, *dashed line*), I_4 ($\beta = 0.2$, *small dashes*), I_5 (*dotted line*). Both rows show on the left hand side polar diagrams of the beaming functions, in the middle the inside components of the beam patterns, and on the right the outside components of the beam patterns.

subject to this caveat. Downward beaming is here modeled by the beaming functions

$$I_3(\delta) = D^3 , \quad I_4(\delta) = D^3 \sin^4 \delta' ,$$
$$I_5(\delta) = \exp\left[- \frac{(\delta - \overline{\delta})^2}{b^2} \right] \tag{9}$$

with the Doppler factor

$$D = \frac{1}{\gamma(1 + \beta \cos \delta)} , \tag{10}$$

where $I_3(\delta)$ corresponds to $I'(\omega', \delta') = \text{const}$ in the rest frame of the matter, $I_4(\delta)$ with δ' determined from

$$\cos \delta' = \frac{(\beta + \cos \delta)}{(1 + \beta \cos \delta)} \tag{11}$$

corresponds to $I'(\omega', \delta') = \sin^4 \delta'$ in the rest frame of the matter, and the Gaussian $I_5(\delta)$ has the parameters $\overline{\delta} = 150°$, $b = 30°$. The specific forms of these beaming functions are chosen ad hoc; they simply serve to illustrate the implication of beamed emission for a range of directions and degrees of beaming that may apply to radiation escaping from the base of an accretion column.

As illustrated in Figure 10, beaming mainly decreases the width of the maxima. Especially in the case of strong downward beaming, each component of the beam pattern may become quite narrow. Therefore beaming may substantially decrease the degree to which the two maxima blend in the combined beam pattern.

The points of disappearance of the inside and outside beam patterns are not affected by beaming. They are determined by the geometric parameters only.

4. DISCUSSION

The beam pattern of a hollow cone has been studied for radial cones of different height and width, for isotropic and beamed emission, and for different values of mass and radius of the neutron star. In this simplified phenomenological model the inside and the outside of the hollow cone radiate up to the radial coordinate r_t, while the upper part of the accretion stream does not radiate. Also, shadowing of the emitting inner side of the column by the upper part of the accretion column has been neglected. In a more detailed model, shadowing should be taken into account. Depending on the accretion rate and the size of the funnel, one should expect scattering in the upper part of the column to alter the inside beam pattern to a greater or lesser degree.

As shown in § 3, a hollow accretion column has a two-component beam pattern that in general exhibits two peaks more or less clearly separated depending on the geometry and on the beaming function. The small-angle component that is due to the inside of the column drops to zero at a viewing angle θ around 100°–110°. The exact location of the zero point depends sensitively on the ratio r_n/r_S of the neutron star and somewhat on the height and width of the column, but not on the beaming function.

This structure closely resembles the features found in the beam patterns that have been reconstructed from pulse profiles of the binary X-ray pulsar Cen X-3 (Fig. 11; Kraus et al. 1996). It is argued below that the properties of the beam patterns suggest an interpretation of this source in terms of hollow accretion columns.

The typical pulse profile of Cen X-3 shows a single peak with a sharp rise and a more gradual decline ending in a shoulder (Fig. 12, *top left*; White, Swank, & Holt 1983). On several occasions a double-peaked pulse profile has been detected at low energies (Fig. 12, *top right*; Nagase et al. 1992). The single-peaked pulse profile is strongly asymmetric, the double-peaked one moderately so. A decomposition analysis of a sample of 12 pulse profiles including the ones shown in Figure 12 has led to the following main results (Kraus et al. 1996): The complete data set is compatible with a scenario according to which the pulse profile from a single emission region is symmetric (or so weakly asymmetric that it does not noticeably contribute to the asymmetry of the observed pulse profile), and where the asymmetry of the observed pulse profile is caused by the nonantipodal location of the magnetic poles. In this

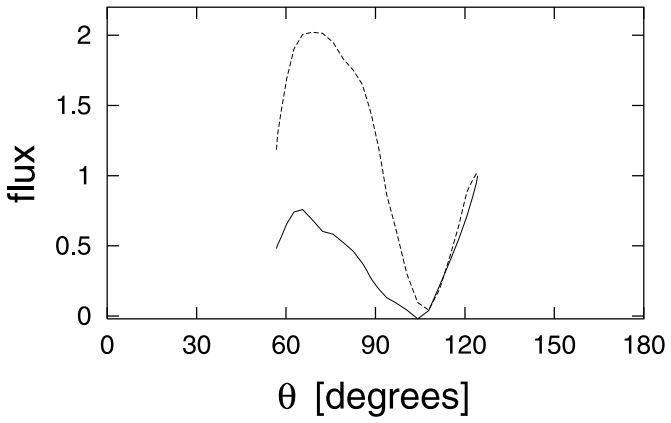

FIG. 11.—Beam patterns that have been reconstructed from the observed pulse profiles of Cen X-3 (Kraus et al. 1996) shown in Fig. 12 top left (beam pattern drawn as a solid line) and top right (beam pattern drawn as a dashed line). The beam patterns are normalized to unity at $\theta = 124°$.

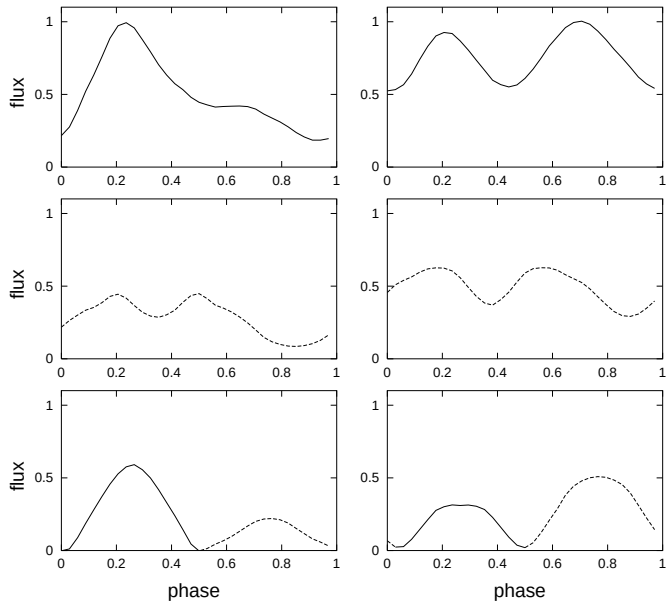

FIG. 12.—*Top row*: two observed pulse profiles of Cen X-3 (White, Swank, & Holt 1983; Nagase et al. 1992). The pulse profiles are normalized so that the flux maximum is unity. *Middle row*: contribution of one emission region to the pulse profile. *Bottom row*: contribution of the other emission region to the pulse profile. The sum of the two contributions gives exactly the pulse profile shown above them. Interpretation of the contributions in terms of hollow accretion columns: flux coming from the outside of a column is drawn in a solid line, flux coming from the inside in a dashed line.

scenario there is only one set of geometric parameters that is acceptable for the whole sample of pulse profiles of Cen X-3: The emission regions are located at $\Theta_1 = 18°$ and $\Theta_2 = 161°$ with respect to the rotation axis and their difference in azimuthal angle is $\Delta\phi = 147°$, which means that there is an offset of 10° between the point that is antipodal to the first magnetic pole and the location of the second magnetic pole. These values are obtained with the assumption that the direction of observation is equal to the inclination of the system $\Theta_o = i = 75°^{+12°}_{-13°}$ (Nagase 1989). The two emission regions have the same beam pattern that in the course of one revolution of the neutron star is sampled for $57° < \theta < 124°$. This visible part of the beam pattern has been reconstructed and consists of two components, the relative size of which varies with energy and between observations. Figure 11 shows the beam patterns that have been deduced from the pulse profiles in Figure 12 and that reproduce these pulse profiles with the geometry given above.[1] These results have been obtained based on symmetry considerations only. There is no model of the emission region involved.

Several of the reconstructed beam patterns show a minimum with (nearly) zero flux (like the ones displayed in Fig. 11 that were chosen for display for this reason), so the two components are well separated and the point at which the flux of the left component drops to zero can be estimated. This zero point coincides very well for different beam patterns, even though the pertinent energy ranges and pulse shapes are quite different, and is located at $\theta \approx 105°$. This value is within the range where the beam pattern from the inside of a hollow accretion column is expected to drop to zero. Since the disappearance of the inner side from view is a geometric effect, the location of the zero point should be independent of photon energy in accordance with what is observed from Cen X-3.

It is therefore plausible to identify the left component of the reconstructed beam pattern with the inside beam pattern of a hollow accretion column. A zero point at $\theta = 105°$ requires $r_n/r_S = 5$ for a small column. This corresponds to a radius of $r_n = 15$ km for a one solar mass neutron star as determined for Cen X-3 (Nagase 1989). (It should be pointed out, however, that the direction of observation Θ_o involves a fairly large uncertainty and that a different value for this angle would predict a different location of the zero point of the left component of the reconstructed beam pattern. Also, substantial shadowing by the upper part of the accretion column would shift the zero point that is predicted for the inside beam pattern towards a smaller value of the viewing angle θ.)

If the right component of the reconstructed beam pattern of Cen X-3 is identified with the outside beam pattern of a hollow accretion column, the emission from the outer side must be beamed downward to produce the observed steep rise in flux (compare with Fig. 10 for the effects of beaming). The inside component shows evidence of beaming as well; the rise in flux below $\theta \approx 65°$ is steeper than it would be for isotropic emission and indicates a comparative lack of radiation emitted upward.

The interpretation in terms of a hollow accretion column is also supported by the spectra derived from the reconstructed energy-dependent beam patterns (Kraus et al. 1996). They show that there are two different spectral regimes corresponding to viewing angles below and above $\theta \approx 100°$, respectively. Such differences in spectrum find a natural explanation if the two components originate in different locations with different physical conditions in general. Conditions on the inside and the outside of the column differ in several important ways. Since the outside is radiating freely whereas the inside is strongly irradiated, one may expect differences in plasma temperature. Also, on the outside the deceleration of the accreted matter may be weaker so that aberration is stronger.

With the geometry given above and when the beam pattern below and above $\theta = 105°$ is attributed to the inside and outside of a hollow accretion column respectively, then the viewing angle onto one emission region varies between $\theta = 57°$ and $\theta = 93°$, so that the observer receives flux only from the inside of this column (Fig. 12, *middle row*), while the viewing angle onto the other emission region varies between $\theta = 86°$ and $\theta = 124°$, so that we see the inside and the outside of the column in turn (Fig. 12, *bottom row*). As illustrated in Figure 12, this means that the main peak of the total pulse profile contains a major contribution from the outside of one of the columns, whereas the shoulder (or the second peak) and the unmodulated flux come from the insides of both columns.

This study has shown that the beam pattern of a hollow cone with two components due to the inside and the outside of the column is quite different from the beam pattern of a solid column. It has more structure than the one-component beam patterns of polar caps, polar rings, or columns. Furthermore, it provides an interpretation of the pulse profiles of Cen X-3.

Thanks to Hanns Ruder, Matthias Stehle, and Steffen Blum for helpful discussions and to Corvin Zahn for the use of his ray-tracing code. This work was partially supported by the DFG.

[1] The decomposition analysis gives the beam pattern only up to the following ambiguity. If $b(\theta)$ is the reconstructed beam pattern, then either $b(\theta)$ or its "mirror image" $\tilde{b}(\theta) = b(180° - \theta)$ is the true beam pattern.

APPENDIX

ANALYTIC BEAM PATTERNS

Analytic beam patterns for emission from the inner or outer sides of a column in the shape of a radial cone with half-opening angle α are computed for $r_S = 0$ (no light deflection) and uniform isotropic emission between radial coordinates r_n (the stellar surface) and r_T (the upper boundary of the optically thick emitting region at the base of the column).

A resolved image of the emission region appropriate for a distant observer is obtained by parallel projection onto a plane perpendicular to the line of sight (defined by the viewing angle θ as illustrated in Fig. 2). For uniform isotropic emission, the total flux observed is proportional to the area that the emitting surface covers in the projected image.

A1. INSIDE BEAM PATTERN

The luminous surface is the inside wall of a radial cone. On the projected image (see Fig. 13), the luminous surface is bounded without by the upper rim of the column that appears as an ellipse with half-axes

$$a_t = r_t \sin \alpha,\ b_t = r_t \sin \alpha \cos \theta\ . \tag{A1}$$

Surrounded by the luminous inside wall is the polar cap of the neutron star that does not emit radiation. If the viewing angle θ is small enough for the polar cap to be in view, then the projection of the polar cap takes up part of the area inside the outer rim ellipse. The polar cap is bounded by a circle of radius $r_n \sin \alpha$ that is projected onto an ellipse with half-axes

$$a_n = r_n \sin \alpha,\ b_n = r_n \sin \alpha \cos \theta\ . \tag{A2}$$

This polar cap ellipse is therefore a second boundary for the luminous projected surface.

The inside of the cone is visible between $\theta = 0$ and $\theta = \pi/2$. This range can be subdivided into three regimes (Fig. 13):

I: For $\theta \leq \alpha$ the entire polar cap ellipse is visible. The projected luminous area is

$$A_I = \pi a_t b_t - \pi a_n b_n\ . \tag{A3}$$

II: For $\alpha \leq \theta \leq \theta_1$ with

$$\tan \theta_1 = \frac{r_t + r_n}{r_t - r_n} \tan \alpha\ , \tag{A4}$$

part of the polar cap ellipse is visible. With the coordinate axes of Figure 13 that are centered in the center of the neutron star, the centers of the ellipses lie at

$$y_t = r_t \cos \alpha \sin \theta,\ y_n = r_n \cos \alpha \sin \theta\ , \tag{A5}$$

respectively, and the ellipses intersect at $(\pm x_1, y_1)$:

$$y_1 = \frac{(r_t + r_n) \sin (\theta - \alpha) \sin (\theta + \alpha)}{2 \cos \alpha \sin \theta}\ , \qquad x_1 = a_n \sqrt{1 - \frac{(y_1 - y_n)^2}{b_n^2}}\ . \tag{A6}$$

The section of the upper rim ellipse that is above $y = y_1$ has the area

$$A_t(y_1) = a_t b_t \arccos\left(\frac{y_1 - y_t}{b_t}\right) - x_1(y_1 - y_t)\ , \tag{A7}$$

and an analogous expression holds for the area $A_n(y_1)$ of the polar cap ellipse above $y = y_1$. The projected luminous area is then

$$A_{\rm II} = A_t(y_1) - A_n(y_1)\ . \tag{A8}$$

III: For $\theta_1 \leq \theta \leq \pi/2$ the polar cap is invisible, being hidden behind the column wall. The luminous area is

$$A_{\rm III} = \pi a_t b_t\ . \tag{A9}$$

The above argument applies if the column is not too broad and/or small. Since the polar cap surface is in the shape of a

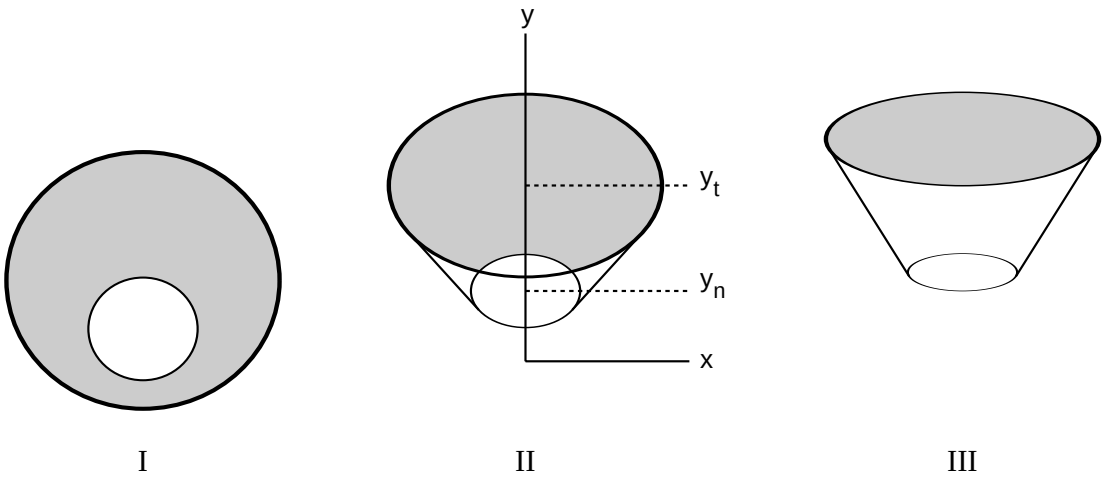

FIG. 13.—Computation of the analytic inside beam pattern: the projected luminous surface (*shaded area*) in regimes I, II, and III. For clarity, the height and width of the cone are greatly exaggerated compared with the model considered in § 2.

section of a sphere, it is elevated above the bounding circle of the polar cap. Viewed from the side, the rear part of the bounding circle may be hidden behind the top of the cap. In this case, the polar cap contributes a boundary to the luminous area that is partly caused by its boundary circle and is partly made up of points on the cap. This case of a composite boundary is excluded if

$$\cos 2\alpha \geq \frac{r_n}{r_t}\,, \tag{A10}$$

in which case the polar cap is entirely hidden behind the column wall for those viewing directions in which a composite boundary would exist.

A2. OUTSIDE BEAM PATTERN

The luminous surface is the outer wall of a radial cone. It is visible between $\theta = \alpha$ and $\theta = \theta_3$, the viewing angle beyond which the column is eclipsed by the star. Eclipse of the whole column is possible if

$$r_t \sin \alpha \leq r_n \tag{A11}$$

and then occurs at

$$\theta_3 = \frac{\pi}{2} + \alpha + \arccos \frac{r_n}{r_t}\,. \tag{A12}$$

This range of viewing angles can be subdivided into four regimes (Figs. 14 and 15):

I: For $\alpha \leq \theta \leq \pi/2$, no part of the luminous surface is eclipsed by the star. The projected luminous surface is bounded above and below by the upper rim ellipse and the polar cap ellipse with sizes and positions as given in equations (A1), (A2), and (A5). It is bounded on the sides by the projections of the generatrix of the cone, which appear as straight lines tangent to both ellipses. The point of contact with the upper rim ellipse, determined from the condition that the tangent to the ellipse at that point is in the radial direction, is $(\pm x_u, y_u)$:

$$y_u = r_t \frac{\cos^2 \alpha \sin^2 \theta - \sin^2 \alpha \cos^2 \theta}{\cos \alpha \sin \theta}\,, \tag{A13}$$

$$x_u = a_t \sqrt{1 - \frac{(y_u - y_t)^2}{b_t^2}}\,, \tag{A14}$$

and an analogous expression holds for the point of contact (x_1, y_1) with the polar cap ellipse (r_t is to be replaced by r_n and a_t, and b_t by a_n, b_n). With the area of the trapezoid with vertices at $(\pm x_u, y_u), (\pm x_1, y_1)$

$$A_T = (x_u + x_1)(y_u - y_1)\,, \tag{A15}$$

of the section of the upper rim ellipse that is below y_u

$$\tilde{A}_t(y_u) = a_t b_t \arccos\left(\frac{y_t - y_u}{b_t}\right) - x_u(y_t - y_u)\,, \tag{A16}$$

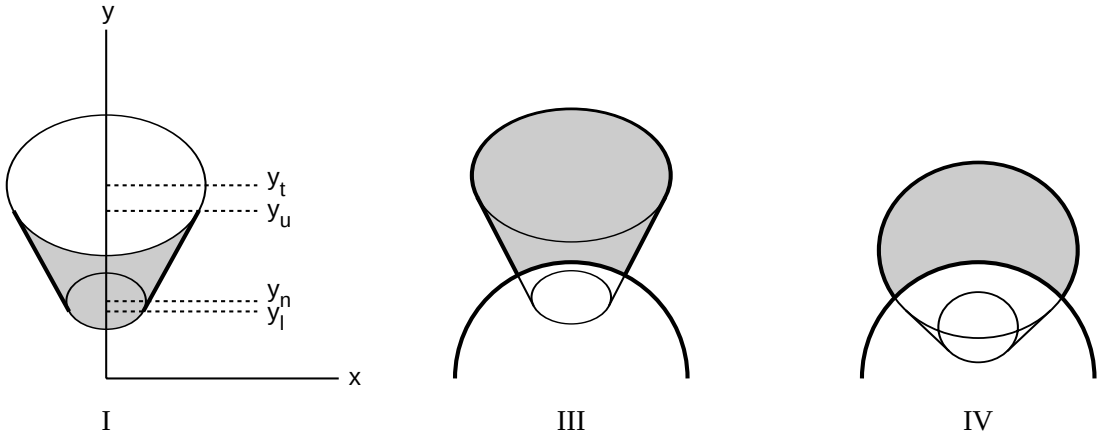

FIG. 14.—Computation of the analytic outside beam pattern: the projected luminous surface (*shaded area*) in regimes I, III, and IV. For clarity, the height and width of the cone are greatly exaggerated compared with the model considered in § 2.

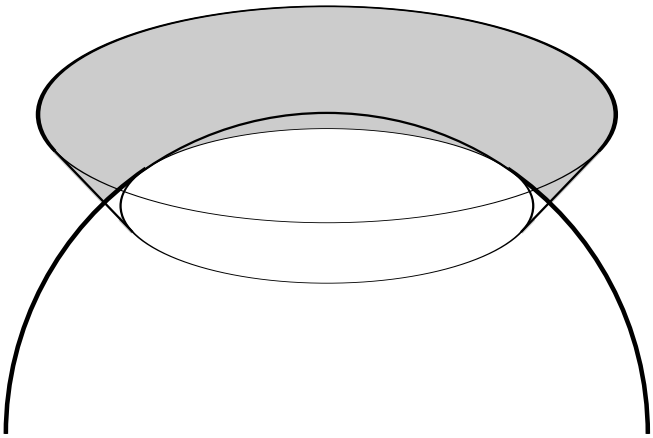

II

FIG. 15.—Computation of the analytic outside beam pattern: the projected luminous surface (*shaded area*) in regime II. For clarity, the width of the cone has been chosen larger (and the height smaller) than in Fig. 14.

and of the section of the polar cap ellipse that is below y_1, $\tilde{A}_n(y_1)$, given by an analogous expression, the area of the projected luminous surface is

$$A_I = A_t - \tilde{A}_t(y_u) + \tilde{A}_n(y_1) \, . \tag{A17}$$

II: For $\pi/2 \leq \theta \leq \pi/2 + \alpha$, the base of the column is partly hidden by the star (Fig. 15). The lower boundary of the luminous projected surface is in the middle given by the polar cap ellipse and on the sides given by the circle that is the projection of the stellar surface. These different sections of the boundary meet at the points of contact of the polar cap ellipse and the stellar circle $(\pm x_2, y_2)$:

$$y_2 = r_n \frac{\cos \alpha}{\sin \theta} \, , \qquad x_2 = \sqrt{r_n^2 - y_2^2} \, . \tag{A18}$$

The upper boundary of the luminous projected surface is defined by the upper rim ellipse as in regime I. If the point (x_u, y_u) is not eclipsed by the star, which is the case if $\theta < \theta_2$ with

$$\theta_2 = \arccos \left[-\sqrt{1 - \left(\frac{r_n}{r_t} \right)^2} \cos \alpha \right] , \tag{A19}$$

then the projection of the generatrix of the cone appears as a boundary to the side. Therefore, under the condition

$$\frac{\pi}{2} + \alpha < \theta_2 \, , \tag{A20}$$

the area of the luminous projected surface in regime II can be calculated from the area of the upper rim ellipse above y_u, $A_t(y_u)$ (eq. [A7]), the area of the triangle with vertices at $(\pm x_u, y_u)$ and (0,0),

$$A_{\rm tr} = x_u \, y_u \, , \tag{A21}$$

the segment of the circle that is contained between the projections of the generatrix of the cone,

$$A_{\rm S} = r_n^2 \arctan \left(\frac{x_u}{y_u} \right) , \tag{A22}$$

the segment of the circle that is between the points of contact with the polar cap ellipse and above y_2,

$$A_{\rm S2} = r_n^2 \arctan \left(x_2 / y_2 \right) - x_2 \, y_2 \, , \tag{A23}$$

and the area of the polar cap ellipse that is above y_2, $A_n(y_2)$ (after eq. [A7]) and is given by

$$A_{\rm II} = A_t(y_u) + A_{\rm tr} - A_{\rm S} + A_{\rm S2} - A_n(y_2) \, . \tag{A24}$$

III: For $\pi/2 + \alpha \leq \theta \leq \theta_2$, the situation is very similar to regime II, except that the lower boundary of the luminous projected surface is simply given by the stellar circle. The area then is

$$A_{\rm III} = A_t(y_u) + A_{\rm tr} - A_{\rm S} \, . \tag{A25}$$

IV: For $\theta_2 \leq \theta \leq \theta_3$ the luminous projected surface is bounded from above by the upper rim ellipse and from below by the stellar circle. The points of intersection between the ellipse and the circle are at $(\pm x_3, y_3)$:

$$y_3 = r_t \frac{\cos \alpha + \cos \theta \sqrt{1 - (r_n/r_t)^2}}{\sin \theta} \, , \qquad x_3 = \sqrt{r_n^2 - y_3^2} \, . \tag{A26}$$

The area of the luminous surface can be calculated from the area of the upper rim ellipse above y_3, $A_t(y_3)$ (after eq. [A7]), and the section of the circle that is above y_3,

$$A_{\rm S3} = r_n^2 \arctan (x_3/y_3) - x_3 y_3 \, , \tag{A27}$$

and is given by

$$A_{\rm IV} = A_t(y_3) - A_{\rm S3} \, . \tag{A28}$$

The above equations are valid under the conditions of equations (A11) and (A20). If one or both of them do not hold, then the calculations for $\theta > \pi/2$ must be modified.

REFERENCES

Arons, J. 1992, ApJ, 388, 561
Arons, J., & Klein, R. 1987, ApJ, 312, 666
Basko, M., & Sunyaev, R. 1976, MNRAS, 175, 395
Becker, P. 1998, ApJ, 498, 790
Foley, J., van Dam, A., Feiner, S., & Hughes, J. 1990, Computer Graphics: Principles and Practice (Reading: Addison-Wesley)
Kirk, J. 1985, A&A, 142, 430
Kraus, U., Blum, S., Schulte, J., Ruder, H., & Mészáros, P. 1996, ApJ, 467, 794
Leahy, D. A., & Li, L. 1995, MNRAS, 277, 1177
Lyubarskii, Y. E., & Syunyuaev, R. 1988, Soviet Astron. Lett., 14, 390
Mészáros, P., & Nagel, W. 1985, ApJ, 299, 138
Misner, C. W., Thorne, K. S., & Wheeler, J. A. 1973, Gravitation (San Francisco: W. H. Freeman)
Nagase, F. 1989, PASJ, 41, 1
Nagase, F., Corbet, R. H. D., Day, C. S. R., Inoue, H., Takeshima, T., & Yoshida, K. 1992, ApJ, 396, 147
Nagel, W. 1981, ApJ, 251, 278
Nollert, H.-P., Ruder, H., Herold, H., & Kraus, U. 1989, A&A, 208, 153
Pechenick, K. R., Ftaclas, C., & Cohen, J. M. 1983, ApJ, 274, 846
Riffert, H., & Mészáros, P. 1988, ApJ, 325, 207
Riffert, H., Nollert, H.-P., Kraus, U., & Ruder, H. 1993, ApJ, 406, 185
Wang, Y.-M., & Frank, J. 1981, A&A, 93, 255
Weiskopf, D. 2000, in IEEE Visualization 2000 Proceedings, ed. T. Ertl, B. Hamann, & A. Varshney (New York: ACM), 445
White, N. E., Swank, J. H., & Holt, S. S. 1983, ApJ, 270, 711
Zahn, C. 1991, Diplomarbeit, Univ. Stuttgart